52.0 – L DATA DRIVEN QUALIFICATION (DDQ) FRAMEWORK FOR METALS ADDITIVE MANUFACTURING

Charles Smith (Mines)
Faculty: Jonah Klemm-Toole (Mines) and Amy Clarke (Mines)
Participant: Craig Brice (Mines)
Sponsor: National Center for Defense Manufacturing and Machining

This project was initiated in January 2021 by the National Center for Defense Manufacturing and Machining. The research performed during this project will serve as the basis for a Master's thesis program for Charles Smith.

52.1 Project Overview and Industrial Relevance

This project aims to solve an inherent problem with additive manufacturing systems. The range of equipment suppliers that use their proprietary feedstock and process parameters makes each AM system and qualification protocol unique. This creates a lengthy qualification process for any new part or material used in manufacturing. This project uses a data-driven qualification approach from relationships across platforms and alloy systems using intelligent machine learning algorithms and physics-based modeling. This project aims to create relationships between solidification velocity, thermal gradients, and microstructure development to help accelerate the qualification and adoption of additive manufactured parts into defense application.

52.2 Previous Work

316L stainless steel was previously acquired as the sponsor specified material for this project. 316L stainless steel exhibits unique solidification behavior, where the primary solidifying phase changes with increasing solidification velocity. Based on the phase diagram, one might assume that 316L would likely experience primary delta ferrite solidification with a solid-state phase transformation into gamma austenite as the material cools. However, in processes that experience fast solidification, such as laser powder bed fusion (LPBF), the primary solidification changes to primary austenite solidification, resulting in a microstructure that contains little to no ferrite in the cooled part [52.1]. This change affects the distribution of sulfur and phosphorus, leading to greater amounts at interdendritic and grain boundary regions, resulting in a greater propensity for solidification cracking. Also, the composition range of 316L stainless steel is quite extensive and slight variations within the accepted range can change the solidification behavior [52.2].

Process parameters of LPBF significantly influence the properties of the as-built material by influencing thermal gradients and solidification behavior. An analytical method to determine ideal process parameters is to use a volumetric energy calculation**, Equation 52.1**. This equation uses laser power (P), scan speed (v), hatch distance (h), and layer thickness (l) to determine the total energy (E_d) the build is exposed to during the LPBF process [52.3]. Results in the literature suggest that the ideal volumetric energy value is in the range of 100 – 105 $\frac{J}{mm^3}$ [52.4]. Materials that are processed using lower values would be more likely to experience increases in porosity, while higher values are likely to experience lower hardness values in the as-built condition [52.4].

$$E_d = \frac{P}{v*h*l} \tag{52.1}$$

Previous work has focused on the development of defect maps that indicate where particular solidification behavior emerges as shown in **Figure 52.1**. These maps use process parameters to predict when keyholing and lack of fusion occur for 316L stainless steel. The Rosenthal model was used to predict the melt pool geometry from process parameters, and geometrical features were combined with analytical models for these defects to generate the map. These maps give approximate values for the occurrence of these defects, but the predictive capability is limited by the assumptions inherent in Rosenthal model [52.5]. The additions of a dimensionless number proposed by Rankouhi accounts for other parameters that are not included in the volumetric energy density calculation. A range of values of this dimensionless number can be plotted on processing maps to provide further guidance for parameter section. The region between the "low end" and "high end" shown in **Figure 52.1** indicate the optimate combinations of laser power and raster velocity to minimize porosity. These maps are made for constant layer thickness and hatch

spacing but provides values for scanning speed and laser power that meet the criteria that is listed above [52.6]. **Figure 52.1** illustrates that although volumetric energy density can provide guidance for parameter section under certain circumstances, if atypical values of hatch spacing and powder layer height are used, volumetric energy density does not provide valuable guidance on parameter selection, as shown by the line of 100 J/(mm^3) extending into the keyholing regime.

52.3 Recent Progress

52.3.1 Analytical Predictive Solidification Model

The first draft of an analytical predictive solidification model for 316L stainless steel has been developed. This model takes the form of a GV map. The foundation of this model is based on the Ivanstov Marginal Stability (IMS) model. This model calculates dendrite tip radius and total dendrite tip undercooling as a function of solidification velocity. These values along with solute diffusivities, bulk concentrations, partition coefficients, and liquidus slopes, regions of planer, cellular, and dendritic growth, the columnar to equiaxed dendrite transition (CET), and lines of equivalent primary and secondary dendrite arm spacing (PDAS and SDAS) can be predicted. The CET was calculated using a criterion proposed by Hunt, as show in **Equation 52.2**, and a relationship between a power law fit of a plot of total undercooling vs solidification velocity and the nucleation undercooling (ΔT_N), as shown in **Equation 52.3** [52.7].

$$G = \frac{1}{n+1}\sqrt[3]{\frac{-4\pi N_o}{3\ln(1-\phi)}}\left(\Delta T\left(\frac{1-\Delta T_N^{n+1}}{\Delta T^{n+1}}\right)\right) \tag{52.2}$$

$$\Delta T = (aV)^{\frac{1}{n}} \tag{52.3}$$

Where a and n are calculated from power law fit, N_o is the number of nucleation sites, ΔT_N is the nucleation undercooling, and ϕ is the fraction of equiaxed dendrites transformed. The primary dendrite arm spacing (PDAS) and secondary dendrite arm spacing (SDAS) are determined from **Equation 52.4** and **Equation 52.5** respectively [52.8].

$$\lambda_1 = \sqrt{\frac{3(\alpha_1 V^{\beta_1})\left(\left(T_L-\alpha_2 V_2^{\beta_2}\right)-T_{base}\right)}{G}} \tag{52.4}$$

$$\lambda_2 = 5.5 M^{\frac{1}{3}} t_f^{\frac{1}{3}} \tag{52.5}$$

Where α_1 and β_1 are the coefficient and exponent of the power law fit for the total undercooling vs solidification velocity. Where α_2 and β_2 are the coefficient and exponent of the power law fit for the tip radius vs solidification velocity. T_L is the equilibrium liquidus temperature of the alloy (for 316L 1440° C was used) and T_{base} is the final solidification temperature calculated from a Gulliver-Scheil simulation (was calculated to be 1207.32° C from Thermocalc at 95% of material solidified). For SDAS calculations, the functions for m and t_f are determined from **Equations 52.6** and **Equations 52.7** respectively [52.8].

$$M = \frac{-\Gamma}{\Sigma\frac{m_j(1-k_j)(c_{f,j}-c_{0,j})}{D_j}} * \ln\left(\frac{\Sigma\frac{m_j(1-k_j)c_{f,j}}{D_j}}{\Sigma\frac{m_j(1-k_j)c_{0,j}}{D_j}}\right) \tag{52.6}$$

$$t_f = \left(\frac{\Delta T_o'}{G*V}\right) \tag{52.7}$$

Where m_j, k_j, D_j, and $c_{0,j}$ are all thermodynamic properties found from the IMS model. $c_{f,j}$ is the final liquid composition at the end of solidification which is found by performing a Gulliver-Scheil simulation. $\Delta T_0'$ is the nonequilibrium freezing range which is the difference between the melting temperature of the alloy (T_L) and the final solidification temperature (T_{base}).

The model, as shown in **Figure 52.2**, will be able to predict the as solidified microstructure if the thermal gradients and solidification velocity are known. The velocity at the transition between primary ferrite to primary austenite was also calculated and determined when the undercooling required for a stable ferrite dendrite exceeds the undercooling required for a stable austenite dendrite. It can be seen that high temperature gradient and low velocity regions at the bottom of the melt pool are expected to solidify as primary ferrite, but a transition is expected as solidification

proceeds in the melt pool. The heat transfer simulation that are described in **Section 52.3.2** are also plotted in the map to show where the process described in **Section 52.3.3** lies and what microstructure is expected from it.

52.3.2 Abaqus Simulations of Moving Heat Source

This project aims to predict microstructure from thermal gradients (G) and solidification velocities (V) during LPBF. Ideally, thermal gradients could be measured during LPBF processing. However, due to the small scale of the melt pool and high travel speeds, such measurements are not currently possible. Accordingly, thermal simulations are the only way to determine G and V at all points in the solid liquid interface during solidification. Abaqus was chosen for this role due to its flexibility and adaptability, allowing the same simulation to be systematically changed to represent different rastering paths and printing techniques. These simulations are done to represent a single moving heat source across a piece of 316L stainless steel, as shown in **Figure 52.3**. Further analysis has started by observing temperatures at predetermined nodes to calculate G and V from the simulations as indicated in **Figure 52.4**. To calibrate the simulation to experimental results the melt pool geometry was matched.

52.3.3 Microstructure Characterization

Microstructure characterization of a thin plate has begun. The plate, **Figure 52.5**, was built as a two-scan path wide plate that has a total width of about 540 µm and was printed using a power of 200 W and a scanning speed of 1400 mm/s. The plate was then sectioned so the cross section is shown and the was polished down to 0.05 µm. The microstructure was exposed by etching with mixed acids that was equal parts hydrochloric, acetic, and nitric acid. The microstructure was observed under a SEM to measure the dendrite arm spacing and observed microstructure. The observations were then compared to the solidification model to start validating the solidification model as seen in **Figure 52.6**.

52.4 Plans for Next Reporting Period

The goals for the next reporting period are as follows:

- Continue validation of solidification model using a verity of different process parameters.
- Observe the range of porosity and microstructure that is present along a constant volumetric energy density to further develop the mesoscale defect map.
- Continue to develop heat transfer simulations to better represent the thermal behavior that is present during a LPBF print.

52.5 References

[52.1] S.A. David, J.M. Vitek, T.L. Hebble, Effect of Rapid Solidification on Stainless Steel Weld Metal Microstructures and Its Implications on the Schaeffler Diagram., Weld. J. (Miami, Fla). 66 (1987). https://doi.org/10.2172/5957599.

[52.2] J. LIPPOLD, Solidification behavior and cracking susceptibility of pulsed-laser welds in austenitic stainless steels, Weld. J. 73 (1994) 129.

[52.3] M. Zhang, C.N. Sun, X. Zhang, P.C. Goh, J. Wei, D. Hardacre, H. Li, Fatigue and fracture behaviour of laser powder bed fusion stainless steel 316L: Influence of processing parameters, Mater. Sci. Eng. A. 703 (2017) 251–261. https://doi.org/10.1016/j.msea.2017.07.071.

[52.4] A. Leicht, M. Rashidi, U. Klement, E. Hryha, Effect of process parameters on the microstructure, tensile strength and productivity of 316L parts produced by laser powder bed fusion, Mater. Charact. 159 (2020) 110016. https://doi.org/10.1016/j.matchar.2019.110016.

[52.5] J.N. Zhu, E. Borisov, X. Liang, E. Farber, M.J.M. Hermans, V.A. Popovich, Predictive analytical modelling and experimental validation of processing maps in additive manufacturing of nitinol alloys, Addit. Manuf. 38 (2021) 101802. https://doi.org/10.1016/j.addma.2020.101802.

[52.6] B. Rankouhi, A. K. Agrawal, F. E. Pfefferkorn, D. J. Thoma, A dimensionless number for predicting universal processing parameter boundaries in metal powder bed additive manufacturing, Manufacturing Letters, Volume 27, 2021, Pages 13-17, ISSN 2213-8463, https://doi.org/10.1016/j.mfglet.2020.12.002.

[52.7] J. D. Hunt, “Steady state columnar and equiaxed growth of dendrites and eutectic,” Mater. Sci. Eng., vol. 65, no. 1, pp. 75–83, 1984, doi: 10.1016/0025-5416(84)90201-5.

[52.8] J. A. Dantzig and M. Rappaz, “SOLIDIFICATION,” in Solidification, 2016, pp. 347–365.

52.6 Figures and Tables

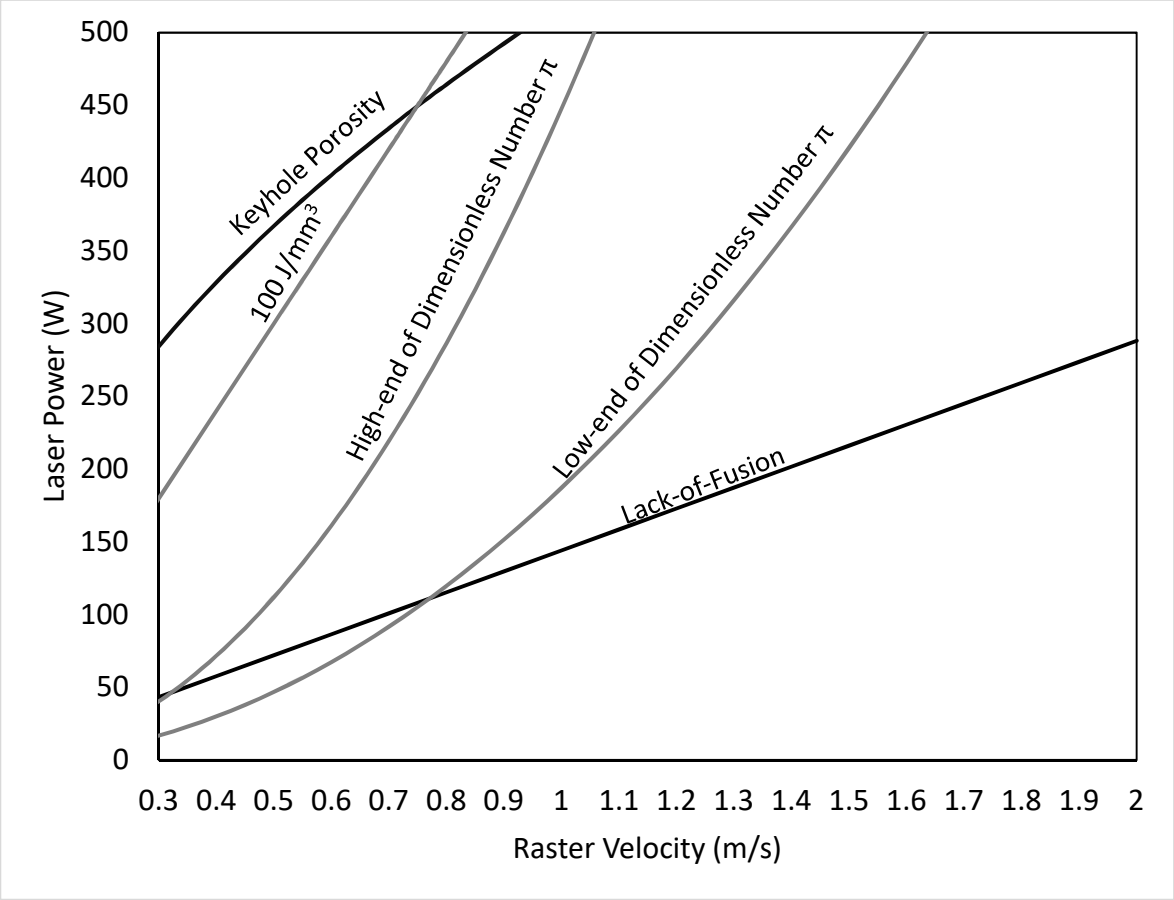

Figure 52.1: Defect map of a constant layer thickness of 60 µm and a constant hatch spacing of 100 µm with a laser spot radius of 50 µm. Line of constant energy density of 100 J/mm3 is plotted to show how even at the same energy density it is possible to move to a defect zone by small changes in process parameters.

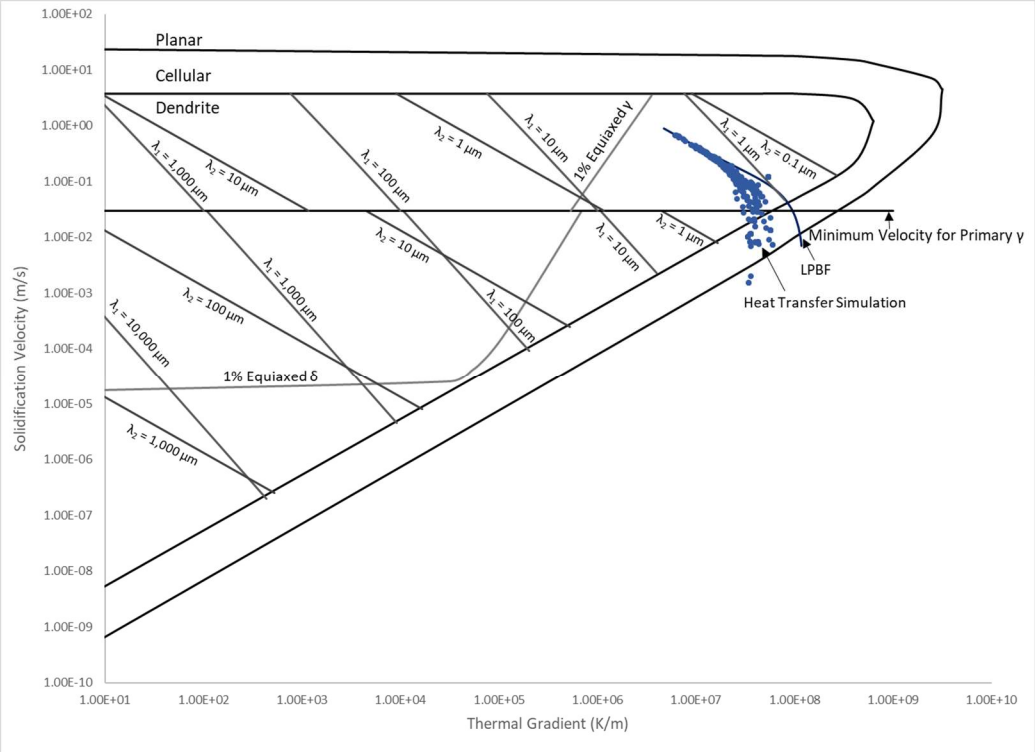

Figure 52.2: Analytical predictive solidification model that take the form of a GV map. The heat transfer simulation result from Section 52.3.2 is plotted to show the predictive microstructure of the process at different sections of the melt pool.

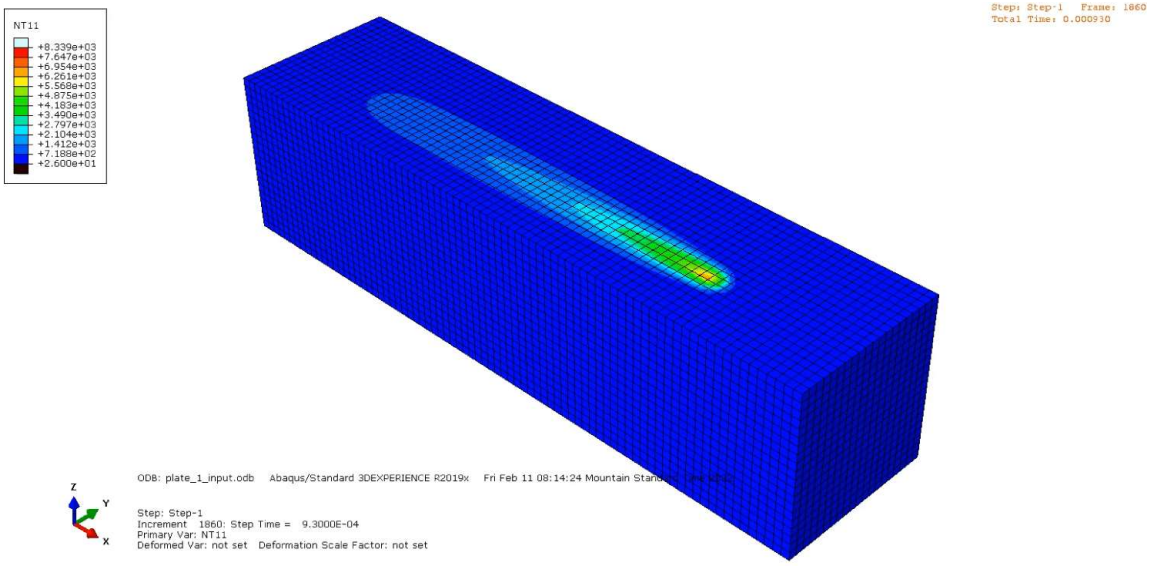

Figure 52.3: A time step in the Abaqus heat transfer simulation of a moving heat source along a piece of 316L stainless steel. The melt pool in the simulation was geometrically matched to that of the experimental build in Section 52.3.3.

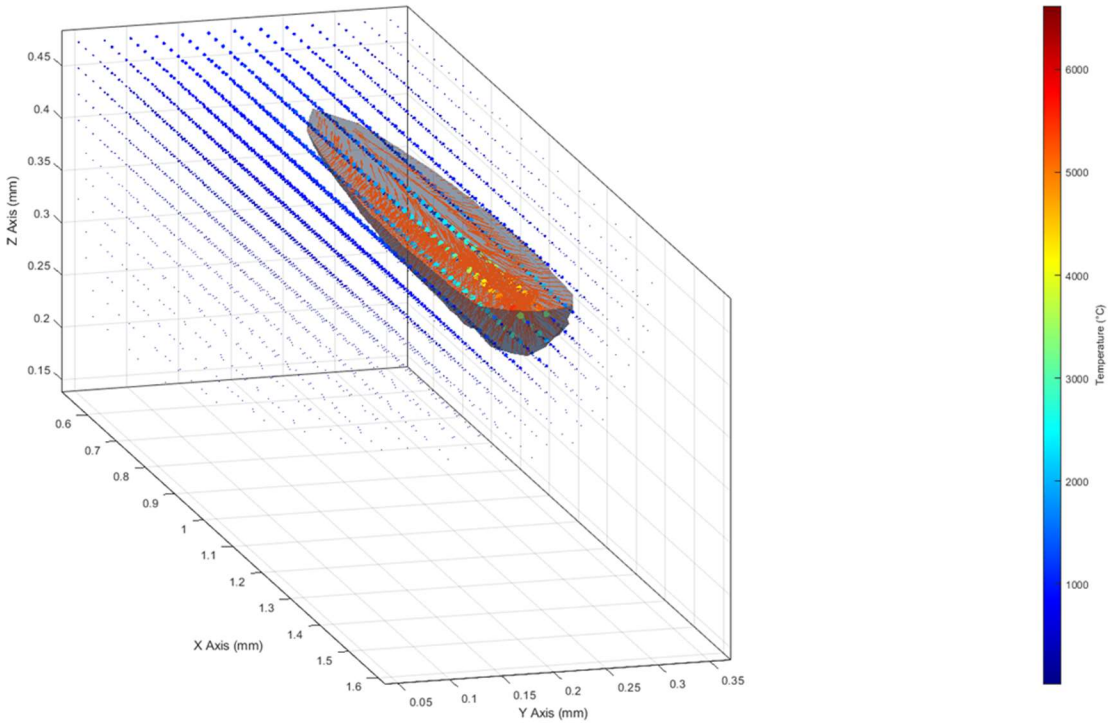

Figure 52.4: The exported thermal data from the Abaqus simulation. An isosurface is drawn at 1440 ºC, the liquidus temperature of 316L, to model the melt pool surface. Normal vectors are plotted along that surface and the magnitude of those vectors is the thermal gradients and by comparing this plot to those of different time steps the cooling rate can be calculated. The solidification velocity can then be determined from the cooling rate and thermal gradient and the results are plotted on the GV map, as shown in Figure 52.2.

Figure 52.5: Thin plate that is about two melt pools in width. The plate is then modeled in Abaqus and the predicted microstructure from the GV map is then compared to the microstructure observed in this plate.

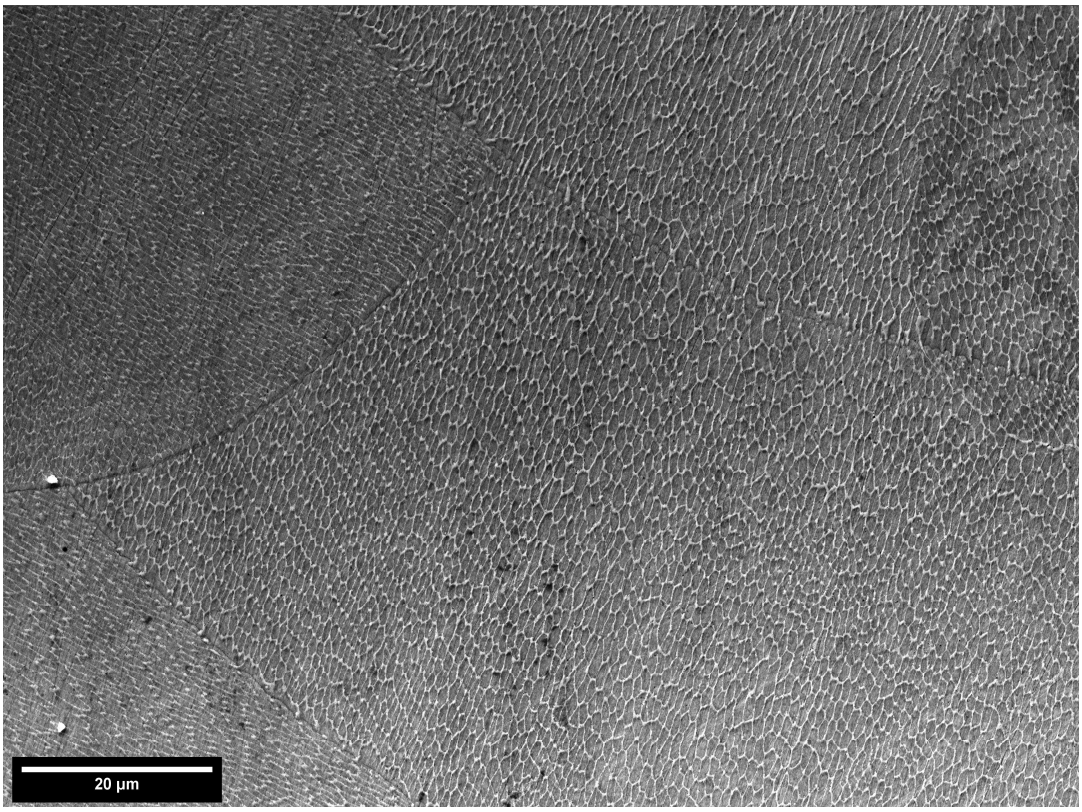

Figure 52.6: Micrograph of the thin plate build taken at 10kx. The average primary dendrite spacing was measured to be 1-2 µm with majority of the microstructure being columnar dendrites and showing no indications of primary ferrite formation.